ADVANCED MATERIALS
www.advmat.de

Enhanced Piezoelectricity of $MAPbI_3$ by the Introduction of MXene and Its Utilization in Boosting High-Performance Photodetectors

Gaosi Han, Xiao-Fen Li, Andy Berbille, Yueming Zhang, Xiongxin Luo, Lindong Liu, Longyi Li, Zhong Lin Wang, and Laipan Zhu**

Recently, perovskite photodetectors (PDs) are risen to prominence due to substantial research interest. Beyond merely tweaking the composition of materials, a cutting-edge advancement lies in leveraging the innate piezoelectric polarization properties of perovskites themselves. Here, the investigation shows utilizing $Ti_3C_2T_x$, a typical MXene, as an intermediate layer for significantly boosting the piezoelectric property of $MAPbI_3$ thin films. This improvement is primarily attributed to the enhanced polarization of the methylammonium (MA^+) groups within $MAPbI_3$, induced by the OH groups present in $Ti_3C_2T_x$. A flexible PD based on the $MAPbI_3$/MXene heterostructure is then fabricated. The new device is sensitive to a wide range of wavelengths, displays greatly enhanced performance owing to the piezo-phototronic coupling. Moreover, the device is endowed with a greatly reduced response time, down to millisecond level, through the pyro-phototronic effect. The characterization shows applying a −1.2% compressive strain on the PD leads to a remarkable 102% increase in the common photocurrent, and a 76% increase in the pyro-phototronic current. The present work reveals how the emerging piezo-phototronic and pyro-phototronic effects can be employed to design high-performance flexible perovskite PDs.

1. Introduction

$MAPbI_3$ is a promising organic-inorganic hybrid perovskite material that has attracted tremendous attention in the field of opto-electronics, such as solar cells, photodetectors (PDs), light emitting diodes, etc.[1–5] This interest is primarily driven by its outstanding properties that include a facile preparation process, high flexibility, adjustable bandgap,[6] high light absorption coefficient,[7,8] low defect density,[9] long lifetime and appropriate diffusion length[10,11] of charge carriers in $MAPbI_3$. Notably, this material can exhibit cubic, tetragonal, or orthorhombic phases, among which the tetragonal phase is the most stable at room temperature while simultaneously possessing superior photovoltaic characteristics.[12] Furthermore, the noncentral symmetry structure imparts piezoelectricity and ferroelectricity to the tetragonal phase.[13,14] Specifically, when a strain is applied on a piezoelectric semiconductor, the induced piezo-charges can effectively tune the energy band structure of the heterojunction or interface, thus further controlling the separation, transportation, and recombination of carriers in the case of light irradiation in $MAPbI_3$. This phenomenon is referred to as the piezo-phototronic effect, which finds great applications in enhancing the opto-electronic performance of perovskites, third-generation semiconductors, two-dimensional (2D) materials, and other materials with noncentral symmetric structures.[15–17] Taking advantage of a strong piezo-phototronic coupling helps realizing

G. Han, X.-F. Li, A. Berbille, Y. Zhang, X. Luo, L. Liu, L. Li, Z. L. Wang, L. Zhu
CAS Center for Excellence in Nanoscience
Beijing Key Laboratory of Micro-nano Energy and Sensor
Beijing Institute of Nanoenergy and Nanosystems
Chinese Academy of Sciences
Beijing 101400, P. R. China
E-mail: zhong.wang@mse.gatech.edu; zhulaipan@binn.cas.cn
G. Han, A. Berbille, Y. Zhang, X. Luo, L. Li, Z. L. Wang, L. Zhu
School of Nanoscience and Engineering
University of Chinese Academy of Sciences
Beijing 100049, P. R. China
X.-F. Li
Key Laboratory of Advanced Materials (MOE)
School of Materials Science and Engineering
Tsinghua University
Beijing 100084, China
Z. L. Wang
Yonsei Frontier Lab
Yonsei University
Seoul 03722, Republic of Korea
Z. L. Wang
School of Material Science and Engineering
Georgia Institute of Technology
Atlanta, Georgia 30332, USA

The ORCID identification number(s) for the author(s) of this article can be found under https://doi.org/10.1002/adma.202313288

DOI: 10.1002/adma.202313288

high-performance in perovskite while preserving their common photoelectric conversion properties. As a result, recent studies have indicated that the piezo-phototronic effect holds the potential for improving perovskite PDs.[21,22] In addition, the pyro-phototronic effect, commonly observed in semiconductors with strong self-polarization,[18–20] presents a promising approach to enhance the performance of PDs. However, the relatively weak self-polarization in $MAPbI_3$ films limits its utilization.

Recently, we witnessed the emergence of a new class of 2D transition metal carbides, nitride and carbonitride, MXenes, with a general formula $M_{n+1}X_nT_x$ (where n = 1, 2, 3, M represents the early transition metal, X is the carbon and/or nitrogen atom, and T_x is the surface termination functional group). These materials have gained significant attraction in various fields such as photocatalysis, medicine, transparent conductors, and battery energy storage due to their exceptional mechanical, thermal, electrical, and optical properties.[23–26] And, in the MXenes family, $Ti_3C_2T_x$ stands out as a prominent example. However, research on utilizing $Ti_3C_2T_x$ to enhance the piezoelectric properties of other materials remains scarce, since Ti_3C_2 (without surface groups) lacks an out-of-plane piezoelectricity due to its central symmetry in the Z-axis direction.[27] Consequently, existing studies on organic/hybrid materials have primarily concentrated on improving the β-phase of PVDF (the strongest piezoelectric phase among the overall five phases) by forming hydrogen bonds to obtain greater piezoelectric outputs.[28] Meanwhile, previous investigations have demonstrated that surface groups of MXene can generate dipoles at the interface between MXene and $MAPbI_3$, which leads to a reduced work function of $MAPbI_3$.[29,30] Based on this evidence, we hypothesize that these enhanced dipoles could also contribute to augmenting the piezoelectric property of $MAPbI_3$ owing to a gain in polarization.

In this study, we fabricated and studied self-powered flexible broadband PDs based on a $Ti_3C_2T_x/MAPbI_3$ heterostructure. Adjusting the ratio of surface groups on $Ti_3C_2T_x$, it leads to a remarkable enhancement of up to 4.27 times in the piezoelectric coefficient compared to that of the sole $MAPbI_3$ thin film. Moreover, the as-fabricated MXene/$MAPbI_3$ also exhibits a significant pyro-phototronic effect, enabling not only an enhancement of the photoelectric responsivity, but also yields to an ultrafast response speed at millisecond-level.[31,32] The synergy created between the piezo-phototronic and pyro-phototronic effects leads to greatly improved performances of self-powered perovskite PDs. Under a 405 nm light irradiation and an applied compressive strain of −1.2%, the current showed an impressive 102% increase in the common photocurrent and 76% concerning the pyro-phototronic current. The strategy we adopted here to further enhance the performance of self-powered perovskite PDs through the pyro-phototronic effect represents an opportunity to bring forward the development of perovskite-based phototronics.

2. Results and Discussion

The perovskite PD is composed of MXene and $MAPbI_3$ light-absorbing layers successively applied by spin coating on an Indium Tin Oxide (ITO) substrate (**Figure 1a**) that serves as a bottom electrode. The Au electrode is then deposited by magnetron sputtering on the exposed $MAPbI_3$ layer. Figure 1b and Figure S1 (Supporting Information) display the schematic structure and optical image of the PD, respectively. For comparison, a control sample without an MXene layer was also prepared. Scanning electron microscopy (SEM) images in Figure 1c,d provide the top view and cross-section of the $MAPbI_3$ layer, respectively, clearly revealing distinct grains boundaries. In Figure 1e, a transmission electron microscopy (TEM) image of the MXene nanosheets presents a smooth topography and a good single crystallinity. Importantly, X-ray diffraction (XRD) spectra displayed in Figure 1f confirms that introducing the MXene layer will not alter the characteristic peaks' positions of $MAPbI_3$. The photoluminescence (PL) spectra presented in Figure 1g shows the introduction of MXene interlayer not only diminishes the intensity of the PL peak, but also induces a blue-shift in the peak from 776 to 763 nm, which can be attributed to an enhancement in electron extraction.[33] UV-visible light absorption spectra (Figure 1h) reveal that the presence of the MXene layer minimally alters the absorption curve of the device, thereby substantiating its exceptional light transmittance.

Piezoresponse force microscopy (PFM) images were obtained to analyze the impact of the presence of $Ti_3C_2T_x$ MXene on the piezoelectric performance of the $MAPbI_3$ film. The morphology analysis (**Figure 2a**) reveals a height fluctuation of 61.6 nm in the $MAPbI_3$ film, while the root mean square (RMS) roughness is 9.62 nm. When combined with the amplitude image (Figure S2, Supporting Information), we found the grain size is ≈300 nm, which is in good consistency with the SEM results. Concurrently, a phase image (Figure 2b) was obtained, showing a significant phase contrast without any apparent correlation to topography. To gain a more intuitive understanding of the polarization effect induced by the tip voltage on the $MAPbI_3$, and confirm the potential derived from the piezoelectric effect in Figure 2b, a large area of perovskite layers was polarized using a bias of −5 V, while highlighting the rest two regions with a bias of +5 V in the phase diagram (Figure 2c). In addition, employing the dual alternating-current (AC) resonance-tracking switching spectroscopy PFM (DART-SS-PFM) hysteresis method reveals the device is endowed with a typical ferroelectric butterfly-shaped ON-field $\overline{\Delta z}$ (vertical piezoelectric deformation) loop.

Meanwhile, a polarization switch occurs at a coercive voltage (direct-current (DC)) of V_{DC} sweeping from -5 to +5 V and the corresponding ON-field $\overline{\Delta z}$ loop presents a typical butterfly shape (Figure 2d) with a slight offset toward negative voltage. This behavior indicates the minor influence of non-ferroelectric artifacts, such as charge injection, which is commonly observed in ultrathin ferroelectric materials.[34] This result demonstrates that both ferroelectric deformation and electrostretching deformation occur when a unidirectional electric field is applied. To investigate the effect of the MXene layer on the piezoelectric coefficient of $MAPbI_3$ film, alternating voltages with different amplitudes (V_{AC}) were applied to the tip of the needle prior to measuring the amplitude of voltage-induced deformation $\overline{\Delta z}$. From these results, and using the formula $d_{33} = \partial(\overline{\Delta z})/\partial V_{AC}$ (Equation (1)), the piezoelectric coefficients before and after adding the MXene layer can be obtained. As shown in Figure 2e, the ITO/$MAPbI_3$ film exhibits a modest piezoelectric coefficient of only 5.66 pm V^{-1}, a value consistent with previous literature.[35] However, upon adding the MXene layer, the piezoelectric

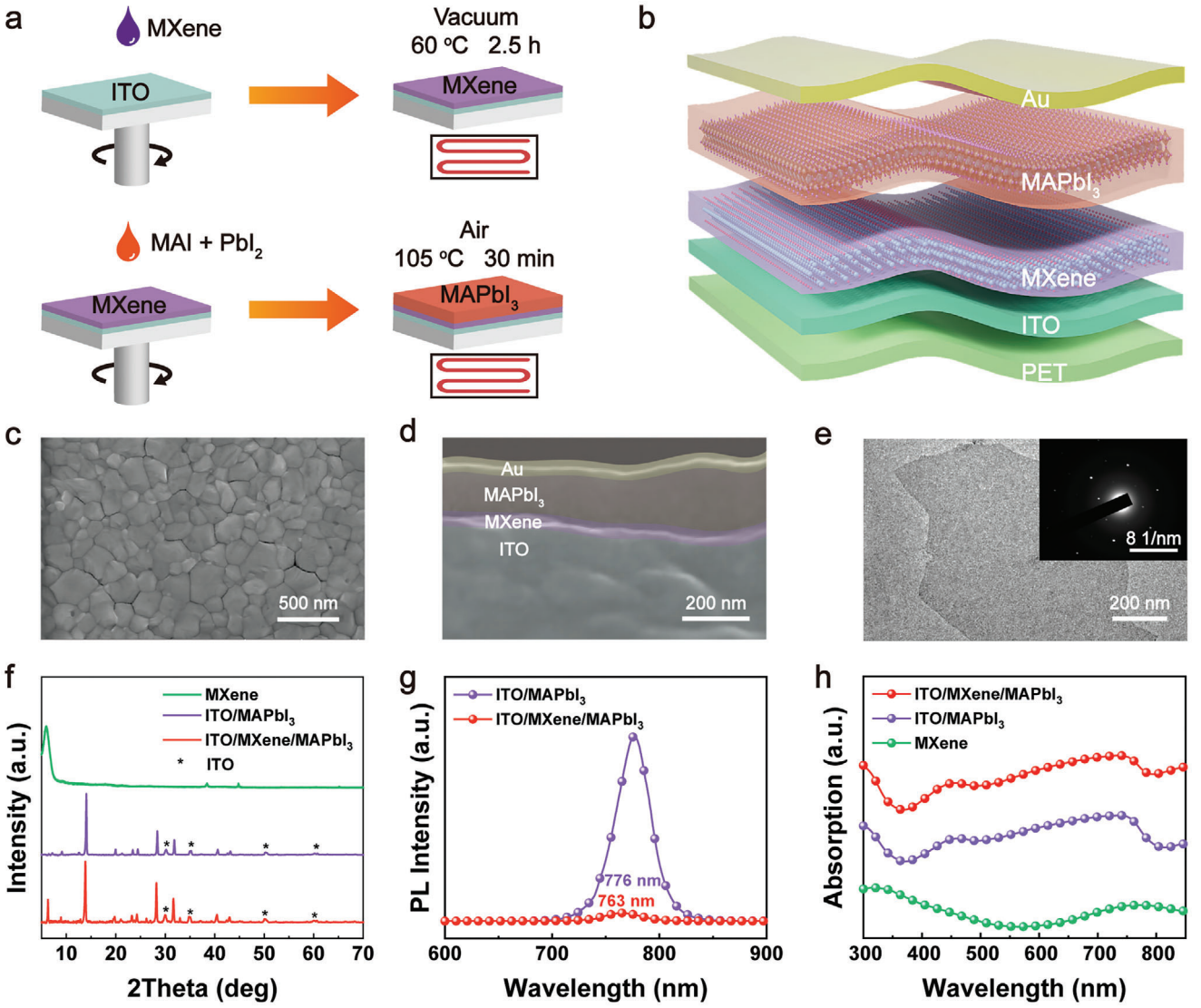

Figure 1. a) Preparation process of the MXene and $MAPbI_3$ layers in the self-powered perovskite PD. b) Structure diagram of the device. c) Top-view SEM image of the $MAPbI_3$ layer. d) Cross-sectional SEM image of the device. e) TEM image of the as-used $Ti_3C_2T_x$ nanosheet. f) XRD patterns of MXene, ITO/MXene, and ITO/MXene/$MAPbI_3$, respectively. g) PL spectra of $MAPbI_3$, MXene/$MAPbI_3$, respectively. h) UV–vis absorption spectra of ITO/MXene/$MAPbI_3$, ITO/$MAPbI_3$, and MXene, respectively.

coefficient significantly increases to 18.28 pm V^{-1}, revealing an enhancement by a factor of 3.23 compared to that of the pristine $MAPbI_3$ layer.

Considering the excellent piezoelectric property of the MXene/$MAPbI_3$ heterostructure film, we then fabricated a flexible piezoelectric nanogenerator. Prior to measuring the piezoelectrically generated charges, we spin-coated a polydimethylsiloxane (PDMS) layer on the bottom surface of the $MAPbI_3$ film, which is then covered by ITO conductive film on the upper surface of the PDMS as an electrode. The overall structure of the device is ITO/MXene/$MAPbI_3$/PDMS/ITO. The PDMS layer functions as a capacitor within the apparatus. Given that $MAPbI_3$ inherently exhibits low resistance (≈200 Ω), there is a propensity for internal short circuits to occur, which can compromise the external power output. By integrating a PDMS layer, it is possible to thwart these internal short circuits while still allowing for the unimpeded flow of electrical charge, that is, enhancing the inner displacement current. In Figure 2f, we observed that under an applied pressure of 0.6 MPa, the current density and the voltage reach up to 0.203 μA cm^{-2} and 3.71 V, respectively, with good linearities within the range from 0.2 to 0.6 MPa (Figure S7, Supporting Information), a significant improvement compared with previous reports.[35] To ensure the output obtained is not an artifact, the current signal is acquired again after the output electrodes are reversed. As shown in Figure 2f, apart from a reversal in the current direction, we did not observe a significant change in the amplitude of the current, thus indicating that the current signals obtained were real.

To understand the mechanism by which MXene enhances the piezoelectric property of $MAPbI_3$, we employed the density

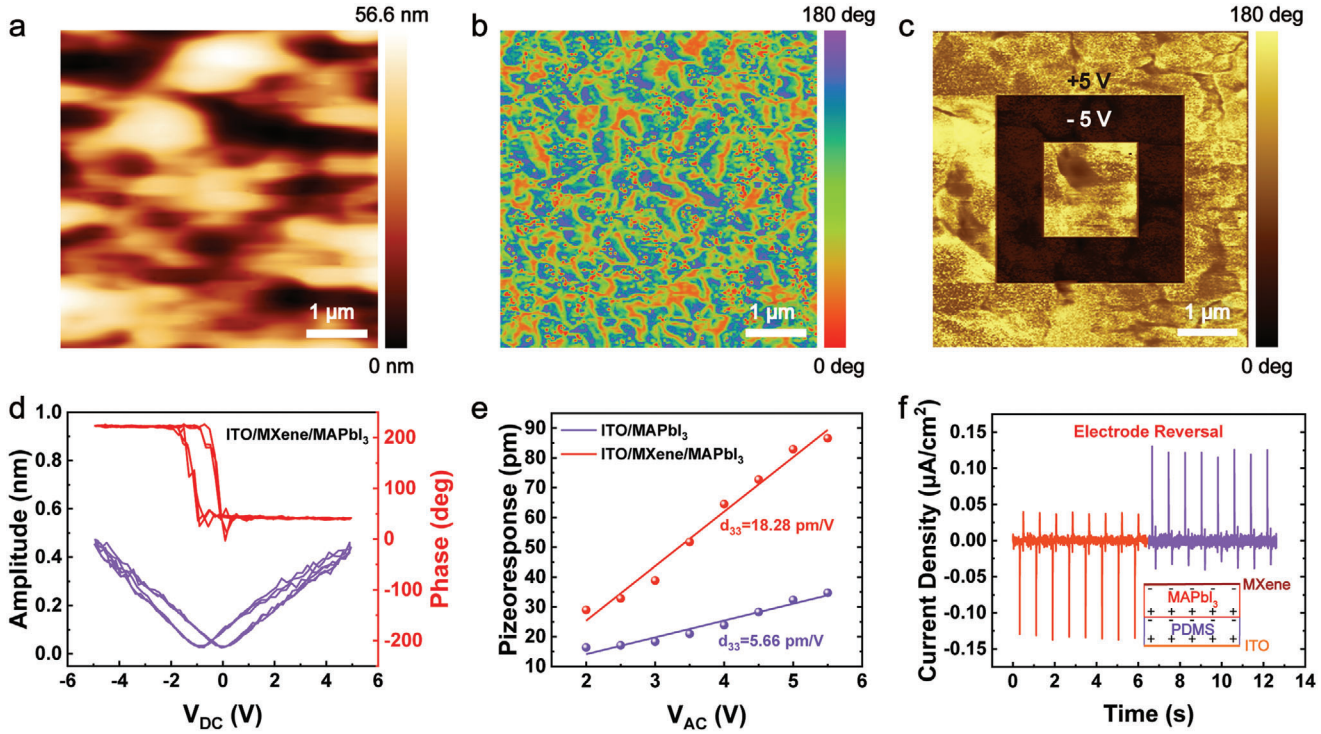

Figure 2. a) An AFM image of the $MAPbI_3$ layer. b) A PFM phase diagram of the $MAPbI_3$ layer. c) The perovskite layer is divided into three sections, where the middle dark region is applied by a voltage of -5 V while the remaining two bright regions by a +5 V voltage. d) Z-axis fluctuation amplitude and phase hysteresis loops by sweeping a DC voltage from –5 to +5 V under a 2.7 V AC driving voltage. e) Average z-axis fluctuation value as a function of driving voltage for the $MAPbI_3$ and MXene/$MAPbI_3$ films, respectively. f) Output of current density obtained from a piezoelectric nanogenerator made with ITO/MXene/$MAPbI_3$/PDMS/ITO under a maximal pressure of 0.2 MPa with positive and negative connections of electrodes.

functional theory (DFT) using the Vienna Ab-initio Simulation Package (VASP) to simulate the changes in the structure of the $Ti_3C_2T_x$ (T = F, O, OH)/$MAPbI_3$ heterojunctions as the composition of the MXene layer changes. Previous studies have demonstrated a strong correlation between the piezoelectric property of the $MAPbI_3$ film and the arrangement of the methylammonium (MA^+, $CH_3NH_3^+$) groups. It has been observed that the piezoelectricity is stronger when the MA^+ groups are more systematically arranged.[36] Therefore, to better describe the orderliness of MA^+, we consider two neighboring MA^+ ions which are closest to the MXene layer, named MA_1 and MA_2. $\angle C_1N_1C_2$ (α) represents the angle formed between the axis along the C_1-N_1 bond of MA_1 and the axis formed by the line between the N_1 atom of MA_1 to the C_2 atom of MA_2. $\angle(C_1N_1\text{-}C_2N_2)$ (β) represents the angle formed by the axis along the C_x-N_x bounds of MA_2 and MA_1. The simulation shows that the F-containing group holds some ways over the organization of MA^+ (**Figure 3a**). Both the angles α and β have some changes compared with the initial values ($\alpha = 88.06°$, $\beta = 0°$, Figure S10, Supporting Information). When paired with the piezoelectric stress constant $\mathbf{e}_{ij}$ matrix (Note S1, Supporting Information), we discovered that the F-containing group can diminish the piezoelectric effect of $MAPbI_3$. This might be attributed to the capability of the F-containing group to spin the MA^+ in a direction opposite to the initial direction of spontaneous polarization. In the $Ti_3C_2O_2$/$MAPbI_3$ structure, a minimal change of the angles α and β can be observed (Figure 3b; Figure S10, Supporting Information), with the angle α only changed by 0.19° and no change for the angle β at all. This result suggests that the incorporation of MXene with O-containing groups does not induce a significant rotation within the MA^+ groups. Such minimal angular change suggests that the presence of O-containing groups should have a negligible impact on the piezoelectricity of $MAPbI_3$. However, we surprisingly found the presence of OH-containing-MXene significantly impacts the lattice structure of $MAPbI_3$. Indeed, not only is the new β angle close to 90°, but we also observe a substantial rearrangement of I atoms (Figure 3c). Given that MA^+ groups are inclined to align on the same side when OH-containing groups are present, we conjecture that the OH groups brought by MXene at the interface with $MAPbI_3$ may be responsible for boosting the piezoelectric property of $MAPbI_3$ in our device.

Despite $Ti_3C_2T_x$ simultaneously comprising of F, O, and OH groups, their relative amounts can be modified, which bestows distinct and tunable properties upon the MXene.[37,38] Nevertheless, such adjustments have minimal impact on the fundamental structure, as confirmed by the XRD patterns shown in Figure 3d. Figure 3e shows Fourier transform infrared (FTIR) spectra of the $Ti_3C_2T_x$ with different group concentrations, with the peaks corresponding to -OH, C-O, and C-F located at 3431, 1622, and 1398 cm^{-1}, respectively. The percentages of these three absorption peaks are extracted in Figure 3f, and the difference in the ratio among groups is clearly visible. This suggests that even though the classifications within the group are not perfectly pure, the d_{33} values calculated

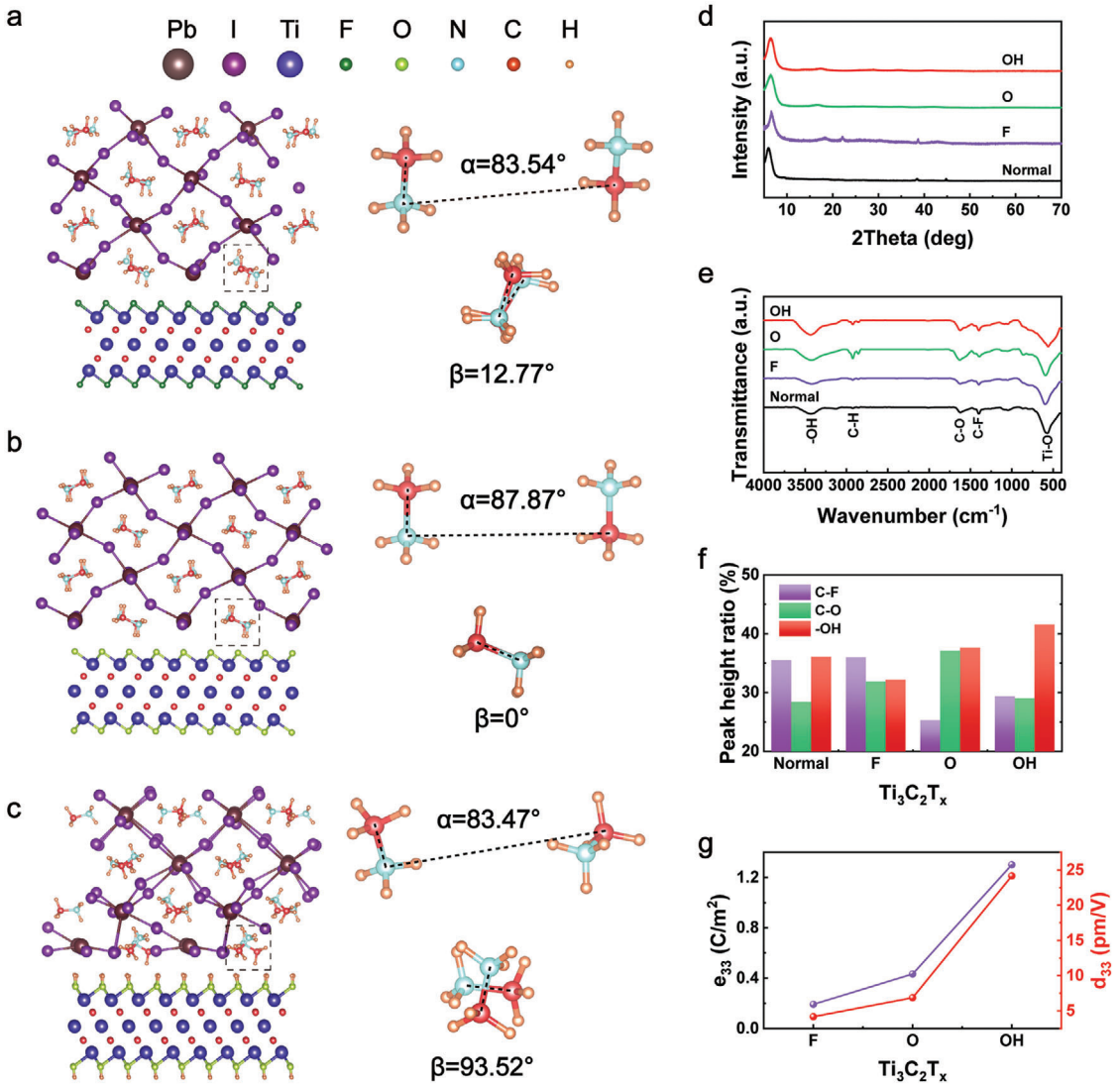

Figure 3. a) $Ti_3C_2F_2/MAPbI_3$, b) $Ti_3C_2O_2/MAPbI_3$, and c) $Ti_3C_2(OH)_2/MAPbI_3$ structure diagrams, and their corresponding C-N angles of one pair of MA^+ in opposite arrangement of $MAPbI_3$. d) XRD patterns of $Ti_3C_2T_x$ with different groups. e) FTIR spectra of different groups of $Ti_3C_2T_x$ colloidal aqueous solutions. f) Height percentage of absorption peaks corresponding to -OH, C-O, and C-F groups of $Ti_3C_2T_x$ in their corresponding FTIR spectra. g) e_{33} calculated by DFT and the measured d_{33} of the $Ti_3C_2T_x$ (T = F, O, OH).

using these classifications still possess a degree of significant reference value. We then measured and calculated the stress-piezoelectric constant e_{33} and the strain-piezoelectric constant d_{33} ($\mathbf{e}_{ik} = \sum_j \mathbf{d}_{ij}\mathbf{C}_{jk}$, $\mathbf{C}_{jk}$ is the elastic constant matrix (Equation (2)), $d_{33} = [(C_{11} + C_{12})e_{33} - 2C_{13}e_{31}]/[(C_{11} + C_{12})C_{33} - 2C_{13}^2]$ (Equation (3))) for the as-used $Ti_3C_2T_x/MAPbI_3$ films (Figure 3g). Since the difference between e_{31} and e_{33} of $Ti_3C_2T_x/MAPbI_3$ is small (see Note S1, Supporting Information), we have chosen to mainly refer to e_{33} to discuss the change of $MAPbI_3$ elastic constant tensor. The d_{33} value of F-containing-MXene/$MAPbI_3$ film is reduced to 4.16 pm V^{-1} compared with that of 5.66 pm V^{-1} for $MAPbI_3$ alone. Meanwhile, the d_{33} value of O-containing-MXene/$MAPbI_3$ film increased to 6.86 pm V^{-1}. Finally, the d_{33} value becomes as high as 24.15 pm V^{-1} for films with OH groups, which greatly surpasses that of ordinary MXene (18.28 pm V^{-1}). The DFT-calculated e_{33} values trend is almost consistent with these observed data.

The enhancement of the piezoelectric properties in the presence of OH groups can be attributed to favorable dipole-dipole interactions in that the C-terminal is drawn toward OH groups, while the N-terminal is pushed away by OH groups. As a result, the dipole moment of MA^+ is now better aligned with the direction of the electric polarization of $MAPbI_3$.[39] Conversely, C-F group exhibits an opposing effect compared to that of OH (ion-dipole interactions). As a result, it induces a rotation of MA^+ to a direction opposing the electric polarization of $MAPbI_3$ itself, ultimately leading to a reduction in piezoelectricity. Even though the $Ti_3C_2T_x$ colloidal aqueous solution with a high concentration of OH group exhibits an enhanced piezoelectric property in the MXene/$MAPbI_3$, it should be mentioned that it also leads to polymerization and precipitation between $Ti_3C_2T_x$ nanosheets due to

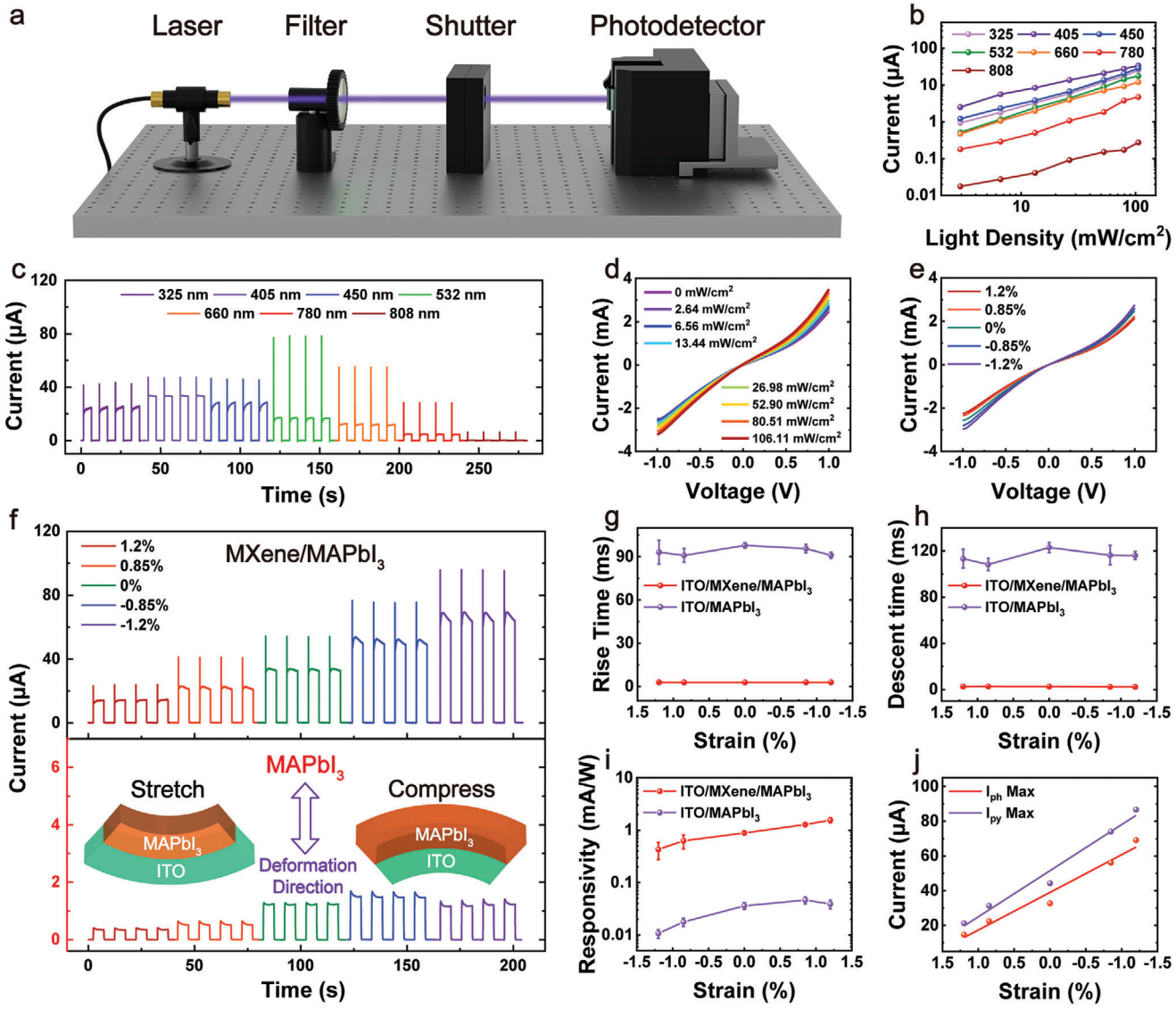

Figure 4. a) Diagram illustration of the light path, encompassing the laser, filter, electronic shutter, and PD in a left-to-right sequence. b) The relationship between photoelectric response and power density of laser under different wavelengths. c) Photoelectric response of the PD under irradiation at different laser wavelengths, where the power densities are normalized to 105.8 mW cm^{-2} with 0 V bias voltage. d) *I-V* curves of the perovskite PD under different light intensities of 405 nm laser. e) *I-V* curves of the perovskite PD under 405 nm laser and different strains. f) Photocurrent of the PD with/without the MXene layer under different strains, using a laser of 405 nm with an intensity of 128.54 mW cm^{-2} with 0 V bias voltage. g) Rise response time and h) Fall response time of the PD with/without the MXene layer. i) Responsivity of the PD with/without the MXene layer. j) The abstracted common photocurrent and pyro-phototronic current under different strains.

the hydrogen bond of OH group. These effects create an uneven surface that affects the spin-coating of the MXene layer, resulting in a significant deterioration of the overall smoothness of the $MAPbI_3$ film. Hence, for device fabrication purposes, we have chosen to work with ordinary $Ti_3C_2T_x$ colloidal water solution instead.

Figure 4a shows a schematic diagram illustrating the optical path used for testing the PD devices based on $MAPbI_3$, or $MAPbI_3$/MXene heterostructure. Prior to experiments, the device was polarized at a DC voltage of 2 V for 0.5 h. The PD is then securely fixed on a bench vice with an adjustable bending degree. Laser light sources with wavelengths of 325, 405, 450, 532, 660, 780, and 808 nm were used to evaluate the output performance of the PD under a 0 V bias voltage. The device presented a high photoelectric output in the range of 325–780 nm, and the current held good linear relationships with the incident laser intensity (Figure 4b). The maximum photocurrent generation is obtained with a 405 nm laser, hence this wavelength was chosen for subsequent measurements (Figure 4c). *I-V* characteristics of the device under various light intensities and varying applied strains are shown in Figures 4d,e. In both experiments, the alterations under both positive and negative voltages present enhanced symmetries, which will be comprehensively further expounded in the text. Additionally, strain dependence of photocurrent was

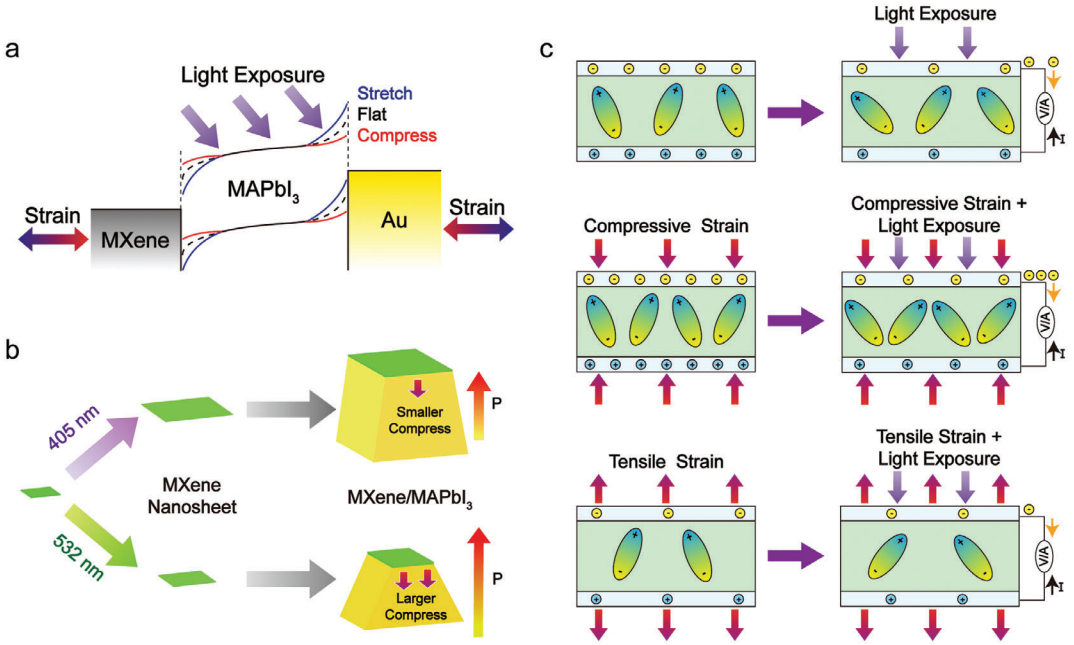

Figure 5. a) Band structure diagram of the device under an applied strain. b) Schematic diagram of greater and smaller pyro-phototronic effects under 532 and 405 nm laser irradiations, respectively. c) Schematic mechanism diagram of the pyro-phototronic current tuned by an applied strain.

investigated by conducting experiments using a PD comprising an MXene layer and a control group without it (Figure 4f). All devices operate at 0 V bias voltage. The incorporation of the MXene layer remarkably improved the photoelectric conversion efficiency due to its capacity not only to enhance electron transmission efficiency, but also to serve as an effective electron transport layer.[40] Simultaneously, the pyro-phototronic current of the device was also greatly improved, and resulted in a significant increase in the photoelectric response speed. Thus, the response time is reduced down to 2 ms (Figure 4g,h). Although the device lacking the MXene interlayer exhibits a current modulation under applied strains, the amplitude of this change is relatively small, and it decreases further under higher compressive strains. On the other hand, the device incorporated with an MXene layer shows a continuous increase in photocurrent, even at a compressive strain of −1.2%. More importantly, the photocurrent responsivity is improved by 102% compared to that without applying a strain (Figure 4i). It is worth noting that applying a strain simultaneously enhances the common photocurrent and the pyro-phototronic current of the PD (Figure 4j). As shown in Figure S19 (Supporting Information), the device still maintains commendable long-term stability.

To account for the change in *I-V* curve under an applied strain observed in Figure 4e, we propose a schematic band structure as shown in **Figure** 5a. This energy band model comprises two back-to-back Schottky barriers, where the right one is for electrons while the left one is for holes. Due to the smaller work function of $Ti_3C_2T_x$ compared to $MAPbI_3$, and the larger work function of Au relative to $MAPbI_3$, the two Schottky barriers exhibit a band-bending in opposite directions. Moreover, when a strain is exerted on the device, polarized charges are induced on either side of the Schottky barrier due to the piezoelectric effect. In general, applying an external compressive strain reduces the energy levels on the $Ti_3C_2T_x$ side while lifting the energy levels on the Au side. Therefore, Schottky barriers are enhanced on both sides, which results in facilitating the flow of electrons on the MXene side and holes flow on the Au side. Meanwhile, applying a tensile strain achieves an opposite result. Hence, the changing trends of the *I-V* curves under strains are almost identical (increase or decrease at the same time) for the forward and reverse voltage regions (Figure 4e).

From Figure 4c, we have seen that the pyro-phototronic current exhibits the largest value under 532 nm light irradiation. However, this phenomenon cannot be simply attributed to photothermal conversion. The analysis of the light absorption spectra (Figure 1h) revealed that the $MAPbI_3$ lacks an absorption peak at 532 nm, and that a minimal change is observed in the absorption spectra before and after incorporating the MXene layer. Therefore, it appeared that the MXene/$MAPbI_3$ heterostructure did not have a particularly prominent photothermal conversion efficiency at 532 nm. It was worth noting that the MXene layer also holds the minimum light absorption near 532 nm, suggesting its limited potential for photothermal conversion at this wavelength. A possible mechanism was proposed considering a photoinduced difference in volume expansion of the MXene nanosheets and $MAPbI_3$ layers, as shown in Figure 5b. The $MAPbI_3$ film possesses a considerable photo-striction coefficient under visible light.[41,42] However, the limited expansion of MXene nanosheets exposed to 532 nm laser irradiation restricts the deformation of the $MAPbI_3$ layer. The significant elasticity of MXene also facilitates the feasibility of this process (MXene: 330 GPa, $MAPbI_3$: 10.4-23.92 GPa).[43,44] When the material bulk expands while its surface is restricted, it experiences a tensile strain along the plane and generates compressive strain internally.[45] As a result, the $MAPbI_3$ preferably deforms on the axis perpendicular to the plane formed by the MXene nanosheets at 532 nm.

This constraint deformation leads to a vertically enhanced piezoelectric polarization of $MAPbI_3$ and a more pronounced pyro-phototronic effect. Potential synergistic contributions from flexoelectricity should not be excluded, as they may also tune the number of polarization charges at the surface of the $MAPbI_3$.

Separating the pyroelectricity from flexoelectricity at ambient conditions may be complex, yet by applying heat to induce the $MAPbI_3$ phase transition at higher temperatures, a photo-induced flexoelectricity can be effectively separated.[46] Notably, the pyro-phototronic and photo-induced flexoelectric currents flow in reverse directions, a finding that corroborates theoretical expectations (Figure S21 and S22, Supporting Information). Simultaneously, directly gauging the strain on $MAPbI_3$ constrained by MXene nanosheets proves to be a challenging task. The optimal approach we envision involves using AFM to detect $MAPbI_3$'s deformation at various elevations above the MXene layer under 405 and 532 nm illumination, however, this approach is far from straightforward. As such, this aspect of the hypothesis requires more rigorous verification.

Figure 5c shows a schematic diagram illustrating the enhancement of the pyro-phototronic effect through the piezo-phototronic effect. The superimposition of electric dipoles results in an enhanced or weakened polarization (spontaneous polarization + piezoelectric polarization). Upon laser irradiation, a fast rate of laser-induced temperature change within the perovskite layer amplifies the oscillation of the electric dipole, subsequently attenuating the spontaneous polarization. This modification then triggers electron migration in the external circuit, leading to a pulsed pyro-phototronic current. When subjected to a compressive strain, a piezoelectric polarization is generated inside the $MAPbI_3$ crystal aligning with the spontaneous polarization, thereby increasing the number of electric dipoles. Consequently, under the same laser irradiation, an intensified oscillation of dipoles occurs, resulting in a stronger pyro-phototronic current. On the contrary, when a tensile strain is applied, the number of dipoles will reduce, leading to a decreased pyro-phototronic current.

3. Conclusion

In conclusion, we have demonstrated the utilization of $Ti_3C_2T_x$ interlayers can effectively enhance the piezoelectric property of $MAPbI_3$ films. This improvement is primarily attributed to the deflection in the polarization of the MA^+ in $MAPbI_3$ induced by the introduction of OH functional groups on the surface of $Ti_3C_2T_x$. The implementation of MXene with a surface rich in OH functional groups has been discovered to increase the d_{33} value of $MAPbI_3$ by 4.27 times compared to that of a sole $MAPbI_3$ film. On this basis, a self-powered flexible PD utilizing an MXene/$MAPbI_3$ heterostructure was fabricated. The PD thus fabricated displays a rapid photoelectric response of millisecond level with a great improvement in performance achieved through both the piezo-phototronic and pyro-phototronic effects. This work not only elucidates the mechanism behind the enhanced piezoelectricity in $MAPbI_3$ thin films with MXene, but also highlights potential applications for high-performance organic-inorganic perovskite PDs enhanced simultaneously by the well-known piezo-phototronic and pyro-phototronic effects.

4. Experimental Section

Materials: The Methylammonium iodide (MAI, 99.5%), Lead(II) iodide (PbI_2, 99.999% metals basis, for Perovskite precursor), *N,N*-Dimethylformamide (DMA, HPLC grade, ≥99.9%), Dimethyl sulfoxide (DMSO, HPLC grade, ≥99.9%), Ethanol (HPLC grade, ≥99.8%), Ethylacetate (99.8%, with molecular sieves, Water ≤ 50 ppm (by K.F.), MkSeal) were procured from Macklin. The $Ti_3C_2T_x$ colloidal aqueous solution (15 mg ml^{-1}) was obtained from Beike Nanotechnology, including F, O, OH group purification and normal. The ITO conductive film (OPV-ITO/PET) was purchased from Pecell. The Polydimethylsiloxane (PDMS, DC184) and its curing agent were sourced from Dow Corning.

Fabrication of the Perovskite PDs: The ITO conductive film (1.5 cm × 1 cm) was rinsed with deionized water and soaked in anhydrous ethanol for 12 h. It was then dried at 60 °C for 10 min, followed by cleaning with ozone plasma for 10 min. The MXene layer was prepared by spinning 50 µL of $Ti_3C_2T_x$ colloidal aqueous solution on an ITO conductive film at 2000 rpm, and subsequently vacuum-dried for 2.5 h. Before the formation of the perovskite layer, the MXene layer underwent treatment with Ar plasma for 10 min, after which the sample was transferred to a glove box filled with N_2 for the perovskite layer. The precursor solution was prepared by stirring MAI (0.48 g), PbI_2 (1.44 g) with DMA (1.92 ml), and DMSO (0.48 ml) together at a temperature of 60 °C for 6 h. Then, the spin-coating procedure made use of 50 µL of a precursor solution, ran at a velocity of 4000 rpm for a period of twenty seconds. When the spin-coating process reached the 10-s milestone, the ethyl acetate antisolvent was promptly added in a dropwise manner. After annealing at 105 °C in air for 30 min, the perovskite crystal structure was formed successfully. The Au electrode layer was obtained through magnetron sputtering under a current intensity of 2 mA for 5 min.

Fabrication of the PENG: Production process of the MXene and perovskite layers was consistent with the PD. Then dropped 100 µL PDMS (PDMS: curing agent = 10:1, vol/vol) on the perovskite layer and spinned for 30 s at 4000 rpm. Immediately afterward, an ITO conductive film (1.5 cm × 1 cm) was promptly affixed to the PDMS layer and cured at 100 °C for 1 h.

Characterization: The microstructure and morphology of the samples were characterized by a field emission scanning electron microscope (SU8020, HITACHI, Japan). The diffraction pattern and atomic arrangement were analyzed using a transmission electron microscope (TEM, Tecnai G2 F20, FEI, USA). PL was measured utilizing a spectrometer (LabRAM HR Evolution, HORIBA, French) with a 325 nm laser. The absorption spectra were obtained by an UV-visible spectrophotometer (UV-3600, Shimadzu, Japan). The X-ray diffraction patterns were recorded employing an X-ray diffractometer (XRD, X'Pert3 Powder, PANalytical B.V, Netherlands). The fourier transform infrared spectroscopy was conducted using a Fourier Transform infrared spectrometer (FTIR, VERTEX80v, Bruker, Germany). The morphology and phase of MXene and $MAPbI_3$ as well as the amplitude, phase and butterfly curves in PFM mode were acquired via an atomic force microscope (MFP-3D-SA, Asylum Research, American). The *I-V* curves of the devices were measured by a semiconductor analysis system (4200-SCS, Keithley, American). The electrical signals were collected and analyzed using a current amplifier (SR570, Stanford, USA).

DFT Calculation: All spin-polarized density functional theory (DFT) computations were performed using the Vienna ab initio simulation package (VASP) based on the projector augmented wave (PAW) method. Electron-ion interactions were described employing standard PAW potentials. A plane-wave basis set with a cutoff kinetic energy of 450 eV was utilized to expand the smooth part of the wave functions. Throughout, for electron-electron exchange and correlation interactions, we employed the Perdew-Burke-Ernzerhof (PBE) functional, which is a form of general gradient approximation (GGA). The Van der Waals interaction was accounted for using the DFT-D3BJ method. In this work, the surface was modeled with a slab model. To ensure proper separation of periodic images, a sufficiently large vacuum region of 15 Å was employed. The Brillouin-zone integrations were conducted using Monkhorst-Pack grids consisting of special points with a separation of 0.05 $Å^{-1}$. A convergence criterion of

10^{-5} eV was set for the electronic self-consistent loop during optimization of atomic structures until residual forces reached below 0.03 eV $Å^{-1}$.

Supporting Information

Supporting Information is available from the Wiley Online Library or from the author.

Acknowledgements

This research was supported by the National Natural Science Foundation of China (52192610 and 52192613), the National Key R & D Project from Minister of Science and Technology (2021YFA1201601), and sponsored by CAS-TWAS President's Fellowship (A.B).

Conflict of Interest

The authors declare no conflict of interest.

Data Availability Statement

The data that support the findings of this study are available from the corresponding author upon reasonable request.

Keywords

$MAPbI_3$, MXene, photodetectors, piezoelectricity, piezo-phototronic effect, pyro-phototronic effect

Received: December 7, 2023
Revised: March 1, 2024
Published online:

[1] Z. Zhao, Y. Li, Y. Du, L. Zhang, J. Wei, F. Lin, *ACS Appl. Mater. Interfaces* **2020**, *12*, 44248.
[2] A. Y. Alsalloum, B. Turedi, X. Zheng, S. Mitra, A. A. Zhumekenov, K. J. Lee, P. Maity, I. Gereige, A. AlSaggaf, I. S. Roqan, *ACS Energy Lett.* **2020**, *5*, 657.
[3] Z. Shi, Y. Zhang, C. Cui, B. Li, W. Zhou, Z. Ning, Q. Mi, *Adv. Mater.* **2017**, *29*, 1701656.
[4] Y. Zhao, F. Ma, Z. Qu, S. Yu, T. Shen, H.-X. Deng, X. Chu, X. Peng, Y. Yuan, X. Zhang, *Science* **2022**, *377*, 531.
[5] S. F. Leung, K. T. Ho, P. K. Kung, V. K. Hsiao, H. N. Alshareef, Z. L. Wang, J. H. He, *Adv. Mater.* **2018**, *30*, 1704611.
[6] C. M. Sutter-Fella, Y. Li, M. Amani, J. W. Ager, F. M. Toma, E. Yablonovitch, I. D. Sharp, A. Javey, *Nano Lett.* **2016**, *16*, 800.
[7] S.-H. Turren-Cruz, M. Saliba, M. T. Mayer, H. Juárez-Santiesteban, X. Mathew, L. Nienhaus, W. Tress, M. P. Erodici, M.-J. Sher, M. G. Bawendi, *Energy Environ. Sci.* **2018**, *11*, 78.
[8] A. H. Slavney, T. Hu, A. M. Lindenberg, H. I. Karunadasa, *J. Am. Chem. Soc.* **2016**, *138*, 2138.
[9] D. Shi, V. Adinolfi, R. Comin, M. Yuan, E. Alarousu, A. Buin, Y. Chen, S. Hoogland, A. Rothenberger, K. Katsiev, *Science* **2015**, *347*, 519.
[10] S. D. Stranks, G. E. Eperon, G. Grancini, C. Menelaou, M. J. Alcocer, T. Leijtens, L. M. Herz, A. Petrozza, H. J. Snaith, *Science* **2013**, *342*, 341.
[11] G. Xing, N. Mathews, S. Sun, S. S. Lim, Y. M. Lam, M. Grätzel, S. Mhaisalkar, T. C. Sum, *Science* **2013**, *342*, 344.
[12] H. Zhang, X. Qiao, Y. Shen, T. Moehl, S. M. Zakeeruddin, M. Grätzel, M. Wang, *J. Mater. Chem. A* **2015**, *3*, 11762.
[13] L. M. Garten, D. T. Moore, S. U. Nanayakkara, S. Dwaraknath, P. Schulz, J. Wands, A. Rockett, B. Newell, K. A. Persson, S. Trolier-McKinstry, *Sci. Adv.* **2019**, *5*, eaas9311.
[14] D. Seol, G. S. Han, C. Bae, H. Shin, H. S. Jung, Y. Kim, *J. Mater. Chem. A* **2015**, *3*, 20352.
[15] Z. L. Wang, *Nano Today* **2010**, *5*, 540.
[16] Z. L. Wang, *Adv. Mater.* **2012**, *24*, 4632.
[17] Q. Yang, X. Guo, W. Wang, Y. Zhang, S. Xu, D. H. Lien, Z. L. Wang, *ACS Nano* **2010**, *4*, 6285.
[18] Y. Zhang, J. Chen, L. Zhu, Z. L. Wang, *Nano Lett.* **2021**, *21*, 8808.
[19] Y. Wang, L. Zhu, Y. Feng, Z. Wang, Z. L. Wang, *Adv. Funct. Mater.* **2019**, *29*, 1807111.
[20] Y. Dai, X. Wang, W. Peng, C. Xu, C. Wu, K. Dong, R. Liu, Z. L. Wang, *Adv. Mater.* **2018**, *30*, 1705893.
[21] F. Khorramshahi, A. G. Woughter, M. K. Ram, I. Kymissis, A. Takshi, *Adv. Electron. Mater.* **2019**, *5*, 1900518.
[22] J. Nie, Y. Zhang, L. Li, J. Wang, *J. Mater. Chem. C* **2020**, *8*, 2709.
[23] P. Kuang, J. Low, B. Cheng, J. Yu, J. Fan, *J. Mater. Sci. Technol.* **2020**, *56*, 18.
[24] K. Rasool, M. Helal, A. Ali, C. E. Ren, Y. Gogotsi, K. A. Mahmoud, *ACS Nano* **2016**, *10*, 3674.
[25] K. Hantanasirisakul, M. Q. Zhao, P. Urbankowski, J. Halim, B. Anasori, S. Kota, C. E. Ren, M. W. Barsoum, Y. Gogotsi, *Adv. Electron. Mater.* **2016**, *2*, 1600050.
[26] Q. Hu, D. Sun, Q. Wu, H. Wang, L. Wang, B. Liu, A. Zhou, J. He, *J. Phys. Chem. A* **2013**, *117*, 14253.
[27] N. A. Shepelin, P. C. Sherrell, E. N. Skountzos, E. Goudeli, J. Zhang, V. C. Lussini, B. Imtiaz, K. A. S. Usman, G. W. Dicinoski, J. G. Shapter, *Nat. Commun.* **2021**, *12*, 3171.
[28] Y. Su, W. Li, X. Cheng, Y. Zhou, S. Yang, X. Zhang, C. Chen, T. Yang, H. Pan, G. Xie, *Nat. Commun.* **2022**, *13*, 4867.
[29] A. Agresti, A. Pazniak, S. Pescetelli, A. Di Vito, D. Rossi, A. Pecchia, M. Auf der Maur, A. Liedl, R. Larciprete, D. V. Kuznetsov, *Nat. Mater.* **2019**, *18*, 1228.
[30] A. D. Vito, A. Pecchia, M. A. d. Maur, A. D. Carlo, *Adv. Funct. Mater.* **2020**, *30*, 1909028.
[31] Z. Wang, R. Yu, C. Pan, Z. Li, J. Yang, F. Yi, Z. L. Wang, *Nat. Commun.* **2015**, *6*, 8401.
[32] Z. Wang, R. Yu, X. Wang, W. Wu, Z. L. Wang, *Adv. Mater.* **2016**, *28*, 6880.
[33] G. Gilliland, *Mat. Sci. Eng. R.* **1997**, *18*, 99.
[34] S. S. Cheema, D. Kwon, N. Shanker, R. Dos Reis, S.-L. Hsu, J. Xiao, H. Zhang, R. Wagner, A. Datar, M. R. McCarter, *Nature* **2020**, *580*, 478.
[35] Y.-J. Kim, T.-V. Dang, H.-J. Choi, B.-J. Park, J.-H. Eom, H.-A. Song, D. Seol, Y. Kim, S.-H. Shin, J. Nah, *J. Mater. Chem. A* **2016**, *4*, 756.
[36] S. Liu, F. Zheng, I. Grinberg, A. M. Rappe, *J. Phys. Chem. Lett.* **2016**, *7*, 1460.
[37] Y. Xie, M. Naguib, V. N. Mochalin, M. W. Barsoum, Y. Gogotsi, X. Yu, K.-W. Nam, X.-Q. Yang, A. I. Kolesnikov, P. R. Kent, *J. Am. Chem. Soc.* **2014**, *136*, 6385.
[38] A. Qian, J. Y. Seo, H. Shi, J. Y. Lee, C. H. Chung, *ChemSusChem* **2018**, *11*, 3719.
[39] J. M. Frost, K. T. Butler, F. Brivio, C. H. Hendon, M. Van Schilfgaarde, A. Walsh, *Nano Lett.* **2014**, *14*, 2584.
[40] L. Yang, D. Kan, C. Dall'Agnese, Y. Dall'Agnese, B. Wang, A. K. Jena, Y. Wei, G. Chen, X.-F. Wang, Y. Gogotsi, *J. Mater. Chem. A* **2021**, *9*, 5016.
[41] T. C. Wei, H. P. Wang, T. Y. Li, C. H. Lin, Y. H. Hsieh, Y. H. Chu, J. H. He, *Adv. Mater.* **2017**, *29*, 1701789.
[42] X. Lv, S. Dong, X. Huang, B. Cao, S. Zeng, Y. Wang, T. Wu, L. Chen, J. Wang, G. Yuan, *Adv. Opt. Mater.* **2021**, *9*, 2100837.

[43] A. Lipatov, H. Lu, M. Alhabeb, B. Anasori, A. Gruverman, Y. Gogotsi, A. Sinitskii, *Sci. Adv.* **2018**, *4*, eaat0491.
[44] Z. Dai, M. C. Doyle, X. Liu, M. Hu, Q. Wang, C. E. Athanasiou, Y. Liu, B. W. Sheldon, H. Gao, S. Liu, N. P. Padture, *Scr. Mater.* **2023**, *223*, 115064.
[45] Z. Feng, W. Choyke, J. Powell, *J. Appl. Phys.* **1988**, *64*, 6827.
[46] C. Quarti, E. Mosconi, J. M. Ball, V. D'Innocenzo, C. Tao, S. Pathak, H. J. Snaith, A. Petrozza, F. De Angelis, *Energy Environ. Sci.* **2016**, *9*, 155.